Inertial Western Boundary Current on a Bottom Slope: Effects of Horizontal Viscosity and Inshore Conditions

HAJIME NISHIGAKI*

Department of Earth Science, Faculty of Education, Oita University, Oita, Japan

(Manuscript received 5 March 1996, in final form 5 May 1997)

ABSTRACT

The author investigates how the path of the subtropical inertial western boundary current on a bottom slope is affected by viscosity, coastal boundary condition, and width of the continental shelf. Steady flow patterns of a weakly viscous homogeneous model are considered. When viscosity is weak and a no-slip boundary condition is given, the boundary current crosses the shelf/slope offshore controlled by the ageostrophic term in the momentum balance so that the velocity change along the path is small. The path is similar to the inertial boundary layer model with a velocity front. It is independent of the viscous coefficient as long as it is weak. When a free-slip condition is given, the boundary current follows the coastline without being detached from the coastline. The width of the shelf changes the nature of the boundary current considerably. For both boundary conditions, two separate jets are made. The offshore jet, which carries most transport of the gyre, tends to follow a contour of f/H. A critical shelf width divides two classifications for each boundary condition. It has a different value for each condition.

1. Introduction

The western boundary current of the subtropical gyre is trapped by the continental slope. Conventionally, this fact is explained by conservation of the potential vorticity of the water column. The potential vorticity $(f + \zeta)/H$ is conserved along streamlines when we ignore dissipation, where f is the planetary vorticity, ζ the relative vorticity, and H the depth. The depth H is not allowed to change significantly because variations of f and ζ are small along streamlines. Therefore, the boundary current roughly follows an isobath. It follows a contour of f/H in linear and weakly nonlinear models. For example, Holland (1967) studied a weakly nonlinear case with a wide bottom slope and found the boundary current following a contour of f/H. Salmon (1992) presented a homogeneous linear solution, which had a boundary current along a contour of f/H. He also considered a linear case using a two-layer analytic model. In his ''Gulf Stream solution,'' the boundary current follows a contour of f/H, where H is the total depth. Although the boundary current is limited to the upper layer that does not touch the bottom, it is controlled by the bottom slope through the condition of uniform lower potential vorticity below it.

Recently, Nishigaki (1995) explained for the first time that the boundary current is trapped by the bottom slope based on the homogeneous inviscid inertial boundary layer. In the inertial boundary layer, the boundary current can cross the slope by large negative relative vorticity canceling a significant decrease of the depth made by the crossing. The path of the boundary current cannot be determined by the balance of the potential vorticity alone. He considered the balance of the momentum along the path as a boundary condition of pressure on a free streamline and proposed a new mechanism on how the path is determined. The western boundary layer, in his model, is assumed to consist of two regions: an offshore active region filled with the gyre water and an inshore stagnant region where there is no motion. They are divided by a velocity front, on which the velocity may be discontinuous but the pressure must be continuous. The position of the velocity front, which is coincident with the path, is determined so that the pressure is continuous on it. Namely, existence of the stagnant region controls the path through the condition of pressure. The flow pattern of his model is shown in Fig. 1. In this paper, the path is defined by the position of the maximum velocity in each east–west section, which may not be a Lagrangean trajectory.

In this study, as an extension of Nishigaki (1995), we investigate cases with horizontal viscosity by examining steady flow patterns of a homogeneous model. The west-

* Current affiliation: Department of Oceanography, The Florida State University, Tallahassee, Florida.

Corresponding author address: Dr. Hajime Nishigaki, Department of Oceanography 3048, The Florida State University, Tallahassee, FL 32306-3048.
E-mail: nishigaki@ocean.fsu.edu

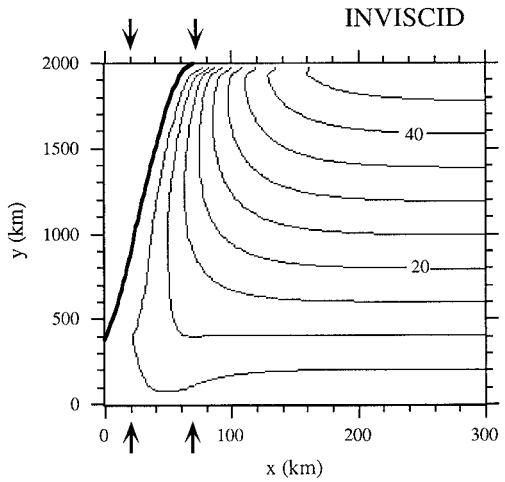

FIG. 1. Flow pattern of the inviscid case of Nishigaki (1995). The streamfunction is in 10^6 m^3 s^{-1}. The arrows point to the ends of the slope. The heavy line is the line of zero streamfunction and the velocity front, which is coincident with the boundary current path.

ern boundary current has wave and eddy motions, which seems to act as turbulent viscosity. So, we investigate how the path is determined when viscosity is present and how it depends on the viscous coefficient. Analysis of the alongpath momentum balance is made and proves to be applicable because the path cannot be determined by the balance of the potential vorticity alone. A no-slip boundary condition is applied to the coast because it seems to make conditions similar to Nishigaki's (1995) model, in which a stagnant region is assumed inshore of the boundary current.

Cases with a free-slip coastal boundary condition are also examined. In no-slip and weakly viscous cases of this study, the supply of momentum and vorticity by the coastal stress seems to detach the boundary current from the coastline and makes an inshore region with weak motion possible. In this study, cases with free-slip conditions are presented to illustrate how the coastal stress affects the boundary current. Studies on the separation of western boundary currents (e.g., Cessi 1991; Haidvogel et al. 1992) show that the choice of the coastal boundary condition shifts the position of separation. In Dengg's (1993) homogeneous Gulf Stream model, the boundary current never leaves the coast when a free-slip boundary condition is used and no cyclonic subpolar gyre is given. It is separated from the coast when the boundary condition is replaced by no-slip. In this study, it is found that the boundary current follows the coastline instead of being trapped by the slope when the free-slip condition and a narrow shelf are given.

How the boundary current depends on the width of the continental shelf is examined in cases with various widths. In the inviscid model of Nishigaki (1995), the boundary current follows the coastline at first, then leaves the coast to cross the shelf/slope offshore. The path across the shelf/slope is adjusted by the stagnant region independent of the shelf width or the coastal position. The position that this path meets the coastline is where the boundary current leaves the coast. However, no solution is found when the shelf is wide so that the path never meets the coastline. Weakly viscous versions of this study with a no-slip coastal condition present similar flow patterns. This suggests that the position where the boundary current leaves the coast is controlled by the path across the shelf/slope, which is independent of the shelf width. So, we examine (i) whether it is true and (ii) if it is, how the boundary current flows when the shelf is wide so that the path never meets the coastline. It is found that the position of detachment is controlled by the path when the shelf is narrower than a critical width. The path tends to follow a contour of f/H when the shelf is wider than the critical width, where f is the planetary vorticity and H the depth.

We summarize the parameter regime of the weakly nonlinear study of Holland (1967), linear study of Salmon (1992), the inviscid study of Nishigaki (1995), and this viscous study. Four parameters are involved: the width L_S of the slope, the width L_M of the horizontally viscous western boundary layer (Munk 1950), the width L_B of the bottom stress western boundary layer (Stommel 1948), and the width L_I of the inertial western boundary layer (Charney 1955; Morgan 1956). The parameters make $L_B = 0$ and $L_I < L_M < L_S$ in Holland (1967), $L_M = L_I = 0$ and $L_B \to 0$ in Salmon (1992), $L_B = L_M = 0$ and $L_I \sim L_S$ in Nishigaki (1995), and $L_B = 0$ and $L_M < L_I \sim L_S$ in this study except for one case in which $L_M \sim L_I \sim L_S$. The streamlines of the boundary current follow contours of f/H in Holland (1967) and Salmon (1992) because L_M, L_B, and L_I are smaller than L_S. In Nishigaki (1995) and this study, they are allowed to cross f/H contours by the nonlinear term since $L_I \sim L_S$. Realistic values for L_I and L_S are both several tens of kilometers, while L_M is around 20 km and L_B is smaller, giving $L_B < L_M < L_I \sim L_S$ as in this study.

2. Numerical model

We set up a numerical model so that the conditions are the same with the inviscid model of Nishigaki (1995) except for horizontal viscosity. The model basin is shown schematically in Fig. 2. The model represents a subtropical western boundary layer. The uniform inflow at the east end represents wind-driven transport, which exits at the north end as an inertial boundary current. Although Nishigaki's (1995) model gives outflow of the free inertial mode (Fofonoff 1954) at the east end, the conditions are essentially the same because the paths of the boundary currents are imposed at the northwest corner. This imposition represents separation of the boundary current, such as the Gulf Stream off Cape Hatteras. We do this because we believe that the mechanism of separation cannot be represented by barotropic models. Sponges are given at the east and north part in order to make the outflow smooth, even when the structure of

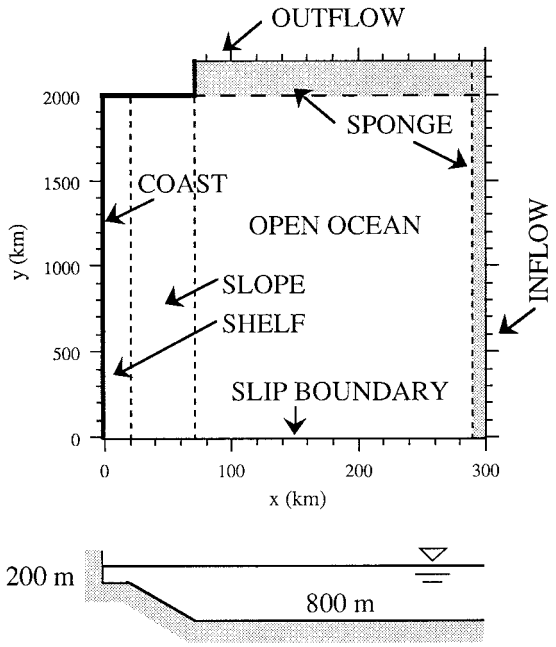

FIG. 2. Schematic illustration of the model basin. The upper panel is the plan view and the lower the cross section. The width of the shelf varies with case.

the boundary current differs from the imposed cutflow and to prevent the boundary from reflecting perturbations coming from the interior.

We use barotropic primitive equations on a beta-plane, namely,

$$u_t + uu_x + vu_y - fv = -\frac{p_x}{\rho_0} + \frac{A_X}{H}(Hu_x)_x + \frac{A_Y}{H}(Hu_y)_y - r(u - u^*) \quad (1)$$

$$v_t + uv_x + vv_y + fu = -\frac{p_y}{\rho_0} + \frac{A_X}{H}(Hv_x)_x + \frac{A_Y}{H}(Hv_y)_y - r(v - v^*) \quad (2)$$

$$(Hu)_x + (Hv)_y = 0, \quad (3)$$

where x and y are eastward and northward coordinates respectively, (u, v) the velocity in (x, y) direction, p the pressure, f the planetary vorticity defined by $f \equiv f_0 + \beta_0 y$, ρ_0 the water density, (A_X, A_Y) the turbulent viscous coefficient in (x, y) direction, r the sponge coefficient (which is nonzero only in the sponge), and (u^*, v^*) the reference velocity in the sponge. The subscripts mean partial differentiation, for example, $u_x \equiv \partial u/\partial x$. The form of lateral viscosity is chosen so that the stress is proportional to the shear and momentum is not produced in the interior. (For example, the form Au_{xx} produces momentum where there is a bottom slope.) The calculations are based on the vorticity equation, which is derived by cross-differentiating the momentum equations (1) and (2),

$$\zeta_t + \{(u\zeta)_x + (v\zeta)_y\} + \beta_0 v + f(u_x + v_y) = D - R, \quad (4)$$

where ζ is the relative vorticity defined by $\zeta \equiv v_x - u_y$, D the horizontal viscous term, and R the sponge term defined by, respectively,

$$D \equiv \left\{\frac{A_X}{H}(Hv_x)_x + \frac{A_Y}{H}(Hv_y)_y\right\}_x - \left\{\frac{A_X}{H}(Hu_x)_x + \frac{A_Y}{H}(Hu_y)_y\right\}_y, \quad (5)$$

$$R \equiv r(\zeta - \zeta^*) - r_y(u - u^*) + r_x(v - v^*), \quad (6)$$

where $\zeta^* \equiv v_x^* - u_y^*$. Boundary conditions are uniform inflow (u) and $v_x = 0$ at the east end; outflow of the inertial boundary current (v) and $u_y = 0$ at the north end; free-slip condition at the south end because the south boundary represents not the coastal boundary but the south end of the subtropical gyre; and either no-slip or free-slip conditions at the coastal boundary, the heavy line in Fig. 2.

We use fine mesh (2 km) in x in order to resolve a viscous layer of ~10 km width sufficiently and coarse mesh (40 km) in y because we are not interested in phenomena with small scales. The planetary vorticity is given for 15° to 30°N, namely, $f_0 = 4.1 \times 10^{-5}$ s^{-1}, $\beta_0 = 2.1 \times 10^{-11}$ m^{-1} s^{-1}. The inflow transport is 5.0×10^7 m^3 s^{-1}. The viscous coefficients A_X and A_Y are 10 m^2 s^{-1} and 10^4 m^2 s^{-1} for most cases, respectively. They are varied in some cases in order to examine the effect of viscosity. A realistic A_X is 10^1 ~10^2 m^2 s^{-1}, as will be mentioned later. In this study, a smaller value is taken as the standard because it is convenient to understand the dynamics. The viscous coefficient A_Y is chosen so that the calculation is made sufficiently stable. The sponge coefficient r is 5.8×10^{-6} s^{-1} (0.5 day^{-1}) at the outer end of the sponge, zero at the inner end, and varies linearly within the sponge. The reference velocity (u^*, v^*) is a uniform westward current in the east sponge and the inertial boundary current in the north sponge. It agrees with the inflow and outflow at the east and north end respectively. Bottom stress is ignored because it does not seem dominant. A typical bottom stress coefficient for the linear law is 5×10^{-4} m s^{-1} (e.g., Chapman and Brink 1987). It makes the stress term ~10^{-7} s^{-1}, where the depth is taken as 500 m and the velocity near the bottom 0.1 m s^{-1}. It is smaller than the advection and the horizontal viscosity of around 10^{-6} s^{-1}, which makes the width of the bottom stress western boundary layer 5 km.

A realistic viscous coefficient is estimated here. The inshore shear zone of the western boundary current on the slope is narrower than the offshore shear zone. In the Gulf Stream, for example, the width of the inshore

TABLE 1. Conditions of each case. A_X and A_Y are viscous coefficients in x and y respectively (in $m^2\ s^{-1}$). BC means coastal boundary condition, in which NS is the no-slip condition and FS the free-slip condition. Width is of the continental shelf (in km). In cases 5 and 7, the width is 20 km in $y = 0 \sim 640$ km and 60 km in $y = 640 \sim 2000$ km.

Case	A_X	A_Y	BC	Width
1	1	5 000	NS	20
2	10	10 000	NS	20
3	100	10 000	NS	20
4	1000	10 000	NS	20
5	10	10 000	NS	20, 60
6	10	10 000	FS	20
7	10	10 000	FS	20, 60
11	10	10 000	NS	30
12	10	10 000	NS	40
13	10	10 000	NS	50
14	10	10 000	NS	60
15	10	10 000	NS	80
23	10	10 000	FS	50
24	10	10 000	FS	60
25	10	10 000	FS	80

shear zone is about 20 km and the width offshore is about 60 km (Richardson et al. 1969; Leaman et al. 1989). The viscous coefficient A is estimated at 10^1 m^2 s^{-1}, assuming that the width $L_M \equiv (A/\beta_0)^{1/3}$ of Munk's (1950) viscous western boundary layer is 10^4 m, where the planetary vorticity gradient β_0 is 10^{-11} m^{-1} s^{-1}. Schmitz and Niiler (1969) estimated the acceleration of the Reynolds stress at 2.5×10^{-6} m s^{-2} in the inshore shear zone of the Gulf Stream at 30°N. This makes the viscous coefficient A at 10^2 m^2 s^{-1} using the equation $A = aL^2V^{-1}$, where a is the acceleration of the Reynolds stress, L the width of the inshore shear zone, and V (1 m s^{-1}) is the typical boundary current velocity. Therefore, a realistic viscous coefficient is $10^1 \sim 10^2$ m^2 s^{-1}.

Conditions for each case are listed in Table 1. Cases 1–4 are a viscous version of Nishigaki's (1995) model with various coefficients. These parameters make the width $L_M \equiv (A_X/\beta_0)^{1/3}$ 3.7, 7.9, 17, and 37 km in cases 1, 2, 3, and 4, respectively, while the width $L_I \equiv (U_0/\beta_0)^{1/2}$ of the inertial western boundary layer (Charney 1955; Morgan 1956) is 39 km in every case, where U_0 is the inflow velocity at the east end. Case 5 has a wider continental shelf between $y = 640$ and 2000 km while the other conditions are the same as in case 2. Cases 6 and 7 are versions with the free-slip coastal boundary condition of cases 2 and 5, respectively. Cases 11–15 are cases with various shelf widths and no-slip coastal boundary. Cases 23–25 are those with free-slip coastal boundary.

This study focuses on steady states although the model includes time evolution. The steady fields are obtained by averaging data of 40 days after an integration of a thousand days, except for cases 1 (averaging 250 days), 4, 6 (no averaging), and 23 (averaging 100 days). In every case the solution is steady enough; the local time change of the relative vorticity ζ_l is no larger than $O(10^{-12}\ s^{-2})$ and smaller than the advection and viscosity by a factor of 10^2. We apply averaging in order to remove periodic waves, which appear on the jet on the slope. These waves have periods of 2–4 days and amplitudes of less than 10^{-10} s^{-2} in ζ_l. They seem to be results of balances between the growth of barotropically unstable waves and dissipation. They appear in every case except for cases 4 and 6. Cases 1 and 23 show weak perturbations, which seem to be short Rossby waves, in the open ocean.

3. Results

a. Effects of horizontal viscosity

We present cases with various viscous coefficients to examine how the horizontal viscosity affects the boundary current. The viscous coefficients of each case are as in Table 1. In cases 1–3, L_M is smaller than L_I, whereas they are comparable in case 4. Steady flow patterns of cases 2 and 4 are shown in Fig. 3. Those of cases 1 and 3 are similar to case 2. The path of the boundary current is defined by the maximum northward velocity v in the east–west section. In every case the boundary current follows the coastline at first, then leaves the coast to be a jet crossing the shelf/slope. The path of each case is shown in Fig. 4 together with the inviscid case of Nishigaki (1995). The paths of the weakly viscous cases 1–3 coincide remarkably north of $y = 1000$ km. This means that the path across the shelf/slope is independent of the viscous coefficient when the width L_M of the viscous boundary layer is smaller than the width L_I of the inertial boundary layer. The paths and the flow patterns are similar to the inviscid case. In case 4, where L_M is comparable to L_I, the boundary current leaves the coast later around $y = 1250$ km and crosses the shelf/slope more abruptly than in the weakly viscous cases. Although variation in A_Y is relatively small among cases 1–4, effective viscosity varies due to dissipation in x.

It is found that the size of the region with weak motion inshore of the boundary current does not affect the boundary current in the weakly viscous case, as that of the stagnant region does not in the inviscid case. In case 5, the continental shelf is widened to 60 km between $y = 640$ and 2000 km; namely, the model basin is as in Fig. 9. The other conditions are the same as in case 2. Streamlines and the path are almost the same as in case 2 (not shown). So, the path is independent of the size of the inshore region with weak motion.

The balance of the alongpath momentum is examined here. The balance consists of four terms: advection, pressure gradient, Coriolis force, and dissipation [cf. Eqs. (1) and (2)]. In the inviscid case, all terms are zero: the advection and the pressure gradient are zero because the velocity and the pressure are constant on the path; the Coriolis term is zero because no flow crosses the path. For viscous cases, the momentum balance on the path across the shelf/slope is shown in Fig. 5. Positive advection means that the flow is accelerated. The other

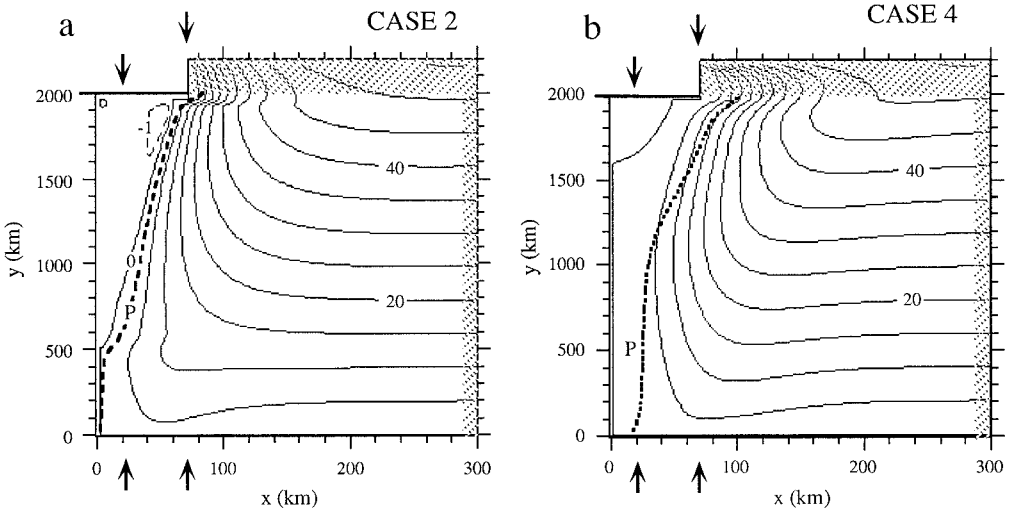

FIG. 3. Flow patterns for cases 2 (a) and 4 (b). The streamfunction is in 10^6 m^3 s^{-1}. The broken lines P show the paths. The arrows point to the ends of the slopes. In both cases, the no-slip condition is given at the coast. The shelf width is 20 km. Viscous coefficients are $(A_X, A_Y) = (10, 10^4$ m^2 s$^{-1})$ in case 2 and $(10^3, 10^4$ m^2 s$^{-1})$ in case 4, respectively.

terms are positive when they accelerate the flow. Namely,

$$\text{(advection)} = \text{(pressure gradient)} + \text{(Coriolis force)} + \text{(viscosity)}. \quad (7)$$

The advection, Coriolis force, and viscosity are calculated by finite differentiations. The pressure gradient is the residual of (7). The Coriolis term is not zero when the streamline crosses the path; it is positive when it crosses the path inshore. It tends to cancel the viscosity in every case.

The momentum balance is examined by considering the ageostrophic force that is defined by the sum of the pressure gradient and the Coriolis force. Conclusions are given briefly here. The appendix has more detailed description. Assuming that (i) the momentum balance in x is geostrophic and that (ii) the pressure gradient along the coast is negligible, the ageostrophic term is given by

$$-p_{P\eta} - fu^* = \frac{f}{H_P}\int_0^{x_P} H_\eta v\, dx - \frac{f}{H_P}\int_0^{x_P} (H_P - H)v_\eta\, dx \equiv X + F, \quad (8)$$

where subscript P means quantity on the path, η is the coordinate parallel to the path, u^* is the velocity component normal to the path, and integrations are done from the coast to the path. Both terms X and F of (8) are concerned with the inshore shear zone of the boundary current which is produced by the viscosity. The term X is the crossing term made by the inshore shear zone crossing the slope. The term F is the profile term, which is concerned with alongpath change of the velocity profile in the inshore shear zone. It is found that X controls the path through a restoring effect to the change of path orientation. The path is controlled so that the velocity variation along it is small. Therefore, the paths of cases 1–3 are similar to the inviscid case.

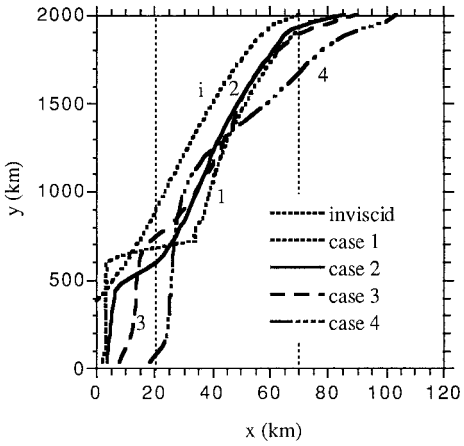

FIG. 4. Paths for cases 1–4 and the inviscid case. The slope lies between $x = 20$ and 70 km.

The ageostrophic forces in the numerical flow patterns are checked here. To estimate the terms of (8), the velocity profiles on the cross-slope sections are shown in Fig. 6 for cases 1–4. A rough estimate of each term is listed in Table 2. The advection A and the viscosity V come from Fig. 5. The crossing term X and the profile term F of (8) are estimated by the inshore shear zone in Fig. 6. In case 1, the boundary current is accelerated by F made by the inshore shear zone narrowing downstream. In cases 2 and 3, which have larger viscous

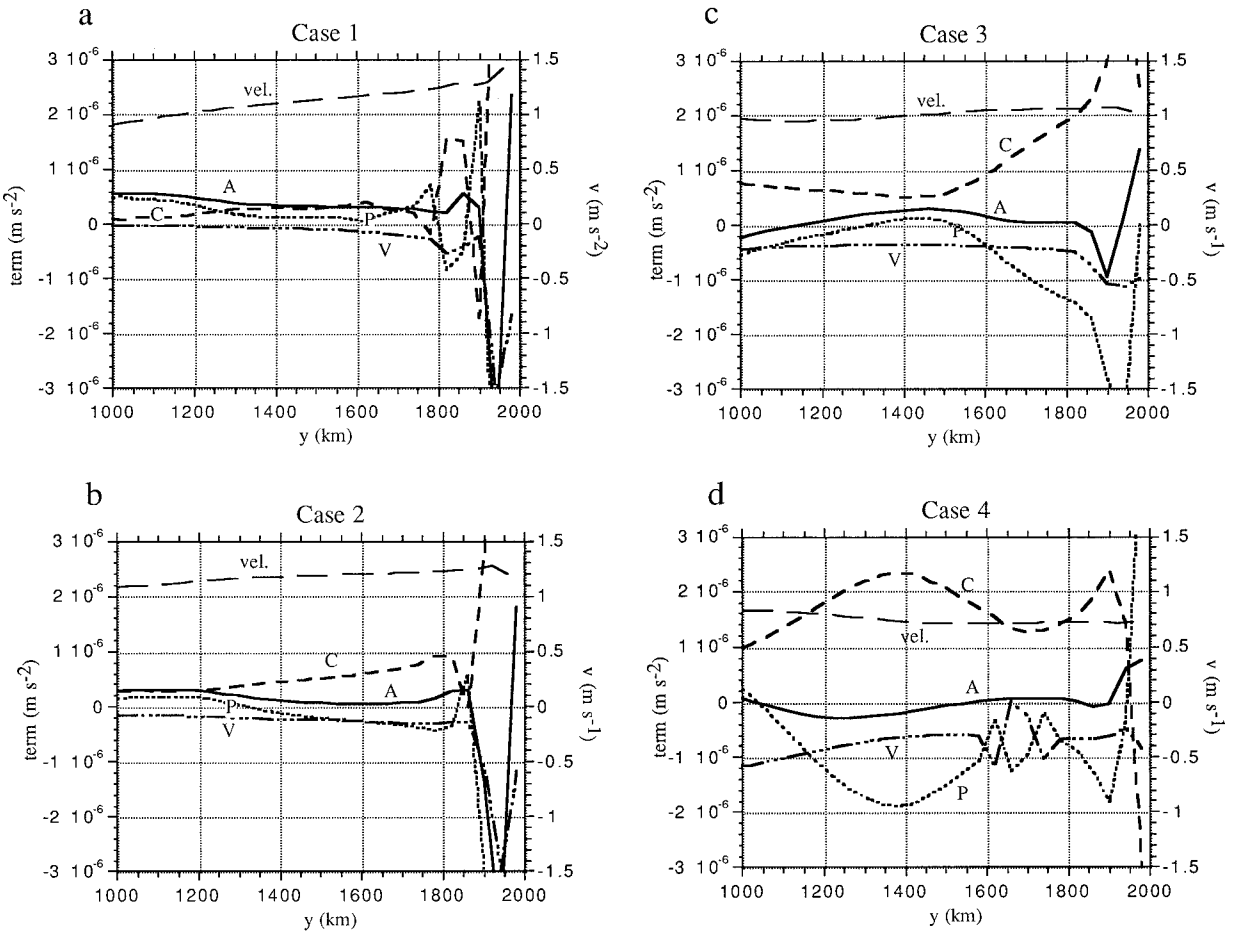

FIG. 5. Alongpath momentum balances along the paths of case 1 (a), 2 (b), 3 (c), and 4 (d). The advection (A), the pressure gradient (P), the Coriolis acceleration (C), and the viscosity (V) are shown. The velocity (vel.) on the path is shown, too.

coefficients, the viscosity V gives larger deceleration. It is supported by an opposing effect of X, which is increased by a wider inshore shear zone. The momentum balance is kept without changing the path. Therefore, the paths of cases 1–3 are very similar. In the intermediately viscous case 4, the balance is different. The inshore shear zone expands downstream, which leads to negative F. The path crosses the slope abruptly to cancel it. A downstream pressure gradient force along the coastline breaks the assumption (ii) and partly cancels negative F. The velocity change along the path remains small.

The vorticity balance on the path is considered. It consists of three terms: advection, beta, and viscosity. Here, the beta term consists of planetary and topographic betas, which show flow crossing the f/H contour. In cases 1–4, both the beta and the viscosity supply positive vorticity, which yields positive advection. Positive advection means that the streamline crosses the path inshore because relative vorticity is almost zero on the path, where curvature of the streamline is small. Since the beta is associated with crossing of the streamline and the f/H contour, crossing of the path and the streamline makes the path crossing the f/H contour.

Distributions of the potential vorticity are examined to consider the effects of viscosity. Potential vorticity distributions of the weakly viscous case 2 and intermediately viscous case 4 are shown in Fig. 7. In case 2, a zone of large potential vorticity is found on the inshore shear zone of the boundary current. From the Lagrangean change of the potential vorticity, a significant supply of positive potential vorticity is seen at the boundary current along the coastline in the south part, consistent with Cessi et al. (1990) in that most of the Lagrangean change of the potential vorticity occurs near the no-slip coast. The positive potential vorticity is carried into the inshore shear zone making a zone of high potential vorticity. In the inviscid case, the inshore stagnant region is assumed. This allows discontinuous velocity and positive infinite potential vorticity, whose source is not considered in the model. In the weakly viscous cases, the line of infinite potential vorticity is replaced by an inshore shear zone with large potential vorticity, which is supplied on the coastal boundary. So,

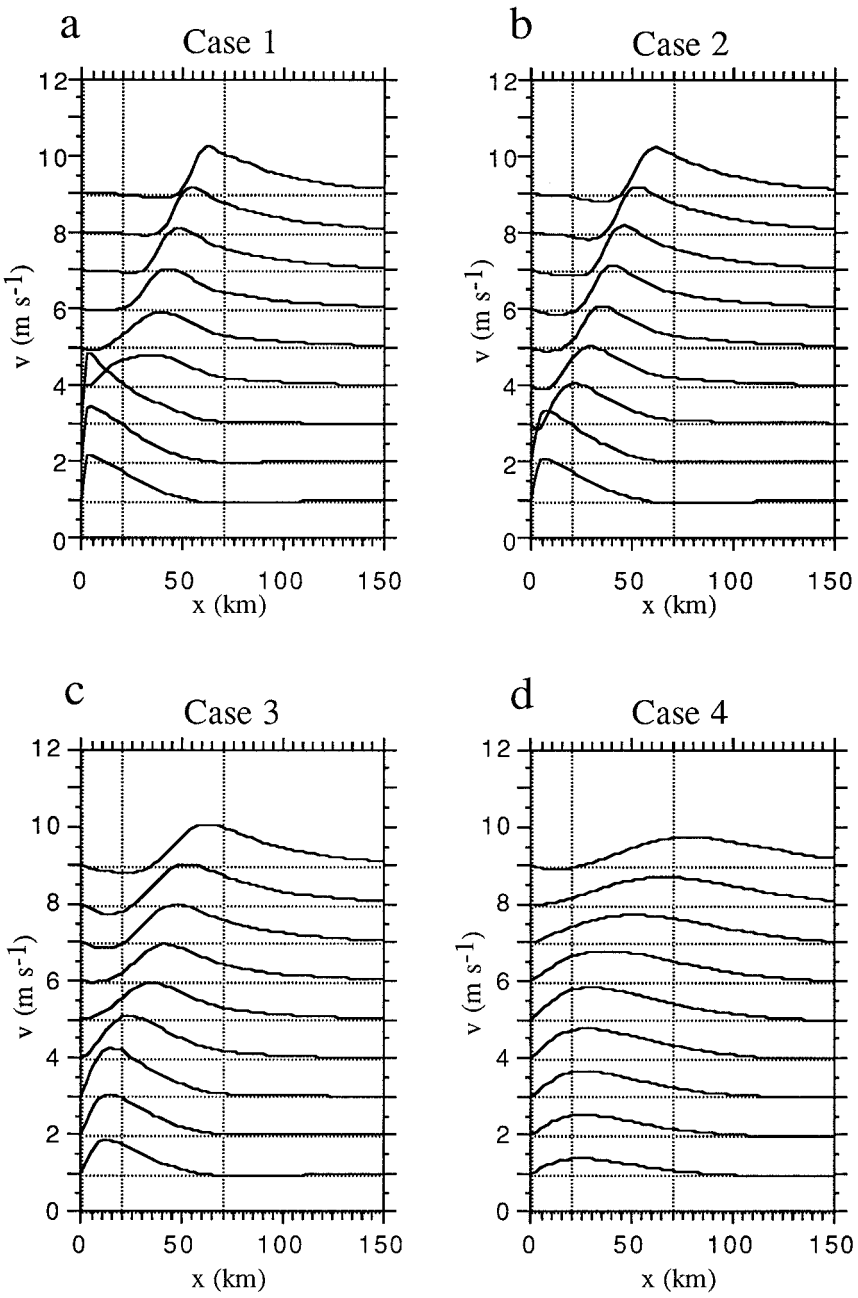

FIG. 6. Profiles of the northward velocity v in the east–west sections for cases 1 (a), 2 (b), 3 (c), and 4 (d). The sections lie every 200 km from $y = 1800$ (top) to 200 km (bottom).

the flow patterns are similar to the inviscid case. This indicates that the potential vorticity supply is critical to the detachment of the boundary current and the existence of the inshore region with weak motion. In the intermediately viscous case 4 (Fig. 7b), the supply of potential vorticity is relatively small. Neither a zone of high potential vorticity nor an inshore region with weak motion is found. This shows that the dynamic nature is different from the weakly viscous cases.

b. Cases with free-slip boundary condition

Case 6 with the free-slip coastal boundary condition is presented in order to examine how the coastal boundary condition affects the path of the western boundary current. Other conditions are the same as in case 2 (Fig. 3a). The flow pattern is shown in Fig. 8. The boundary current is trapped not by the slope but by the coastline. It is drastically different from case 1. This flow pattern almost coincides with the inertial western boundary cur-

TABLE 2. Rough estimates of the terms in the momentum balance on the path. *A*: the advection, *X*: the cross term, *F*: the profile term, and *V*: the viscosity.

	Case 1		Case 2		Case 3		Case 4
A	+	>	+	>	+	>	+
X	+	<	+	<	+	<	+
F	+	>	0	~	0	>	−
V	0	>	−	>	−	>	−

rent (Fig. 18a). The steady fields of cases 2 and 6 are independent of the initial condition of the numerical integration. They are steady flow patterns for respective boundary conditions. In case 2, the boundary current gets negative momentum and positive vorticity from the no-slip coast in the south part and is detached from the coastline. In case 6, however, no factor decelerates the boundary current along the coastline since no stress works on the coastal boundary. So, the boundary current cannot leave the coastline. Similar flow patterns are also found in the inviscid model (Nishigaki 1995) as solutions for two boundary conditions. The boundary current is trapped by the slope when the inshore boundary condition assumes a stagnant region. It follows the coastline when no stagnant region is assumed. Results of case 2 and 6 are consistent with Cessi (1991) and Haidvogel et al. (1992) in that the boundary condition affects the boundary current separation. Although the difference between cases 2 and 6 seems too significant, it is consistent with Dengg's (1993) result in which the boundary current never leaves the coast when a free-slip coast is used and no subpolar gyre is given.

The factor that detaches the boundary current from the coastline is not always the coastal stress. For example, case 7 is presented with the free-slip boundary condition and an expanded shelf between $y = 640$ and 2000 km. Its flow pattern is shown in Fig. 9. The boundary current leaves the coastline by an overshoot at the headland at $y = 640$ km to cross the shelf/slope. The path agrees with case 2 north of $y = 1000$ km. This indicates that whether the boundary current is on the slope or along the coastline depends on the existence of a factor that detaches the boundary current from the coastline. Case 7 is not consistent with Dengg's (1993) result. Strong nonlinearity of this model makes the detachment possible by the supply of positive vorticity in a thin viscous layer.

c. *Dependence on the shelf width for the no-slip boundary condition*

How the boundary current path depends on the shelf width is examined for the no-slip boundary condition. It is found that the flow patterns for various shelf widths can be classified into two groups. When the shelf is narrow, the flow pattern is similar to case 2. The boundary current is a connected jet that follows the coastline in the south part and crosses the shelf/slope offshore afterward. When the shelf is wide, the flow pattern is similar to case 15 (Fig. 10), which we make the standard of the case with a wide shelf and no-slip coastal condition. The flow in the southwest corner along the coastline immediately leaves the coastline and turns offshore. However, another disconnected jet is found on the slope, which carries most the gyre volume transport. Paths for various shelf widths are shown in Fig. 11. In this paper, the path is drawn where the velocity exceeds 0.2 m s^{-1}. The paths for cases with narrow shelves, case 2, 11, and 12, agree quite well across the shelf/slope. In cases 14 and 15, the paths on the slope are closer to an *f*/*H* contour. Case 13 has an intermediate path.

The alongpath momentum balance along the path is

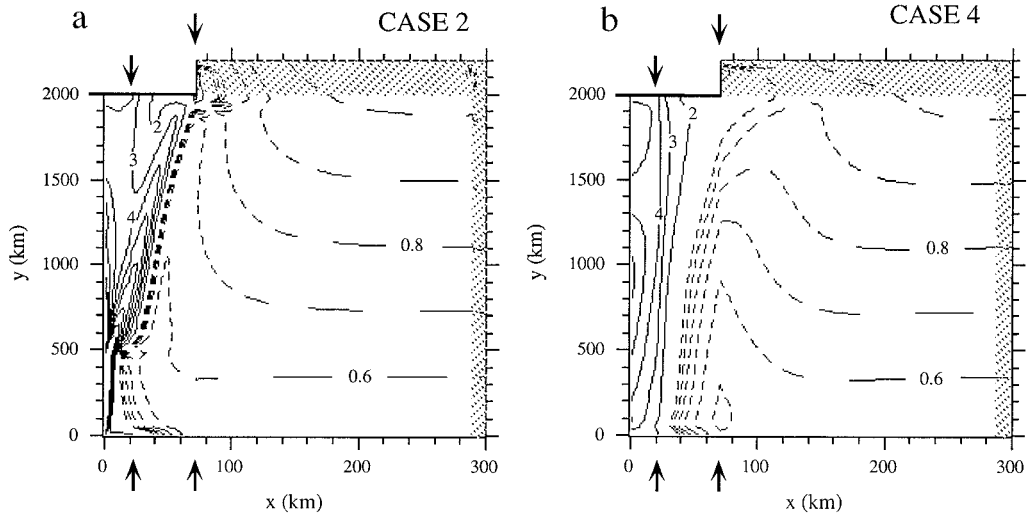

FIG. 7. Distributions of the potential vorticity for case 2 (a) and 4 (b). The potential vorticity is in 10^{-7} m^{-1} s^{-1}. In both cases, the no-slip condition is given at the coast. The shelf width is 20 km. Viscous coefficients are (A_X, A_Y) = (10, 10^4 m^2 s^{-1}) in case 2 and (10^3, 10^4 m^2 s^{-1}) in case 4, respectively.

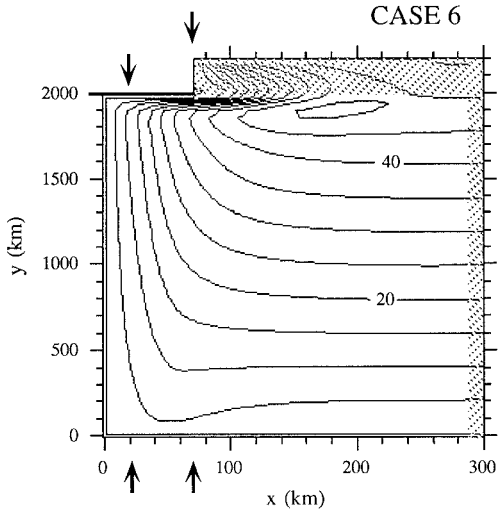

FIG. 8. Flow pattern for case 6. Free-slip condition is given at the coast. The shelf width is 20 km.

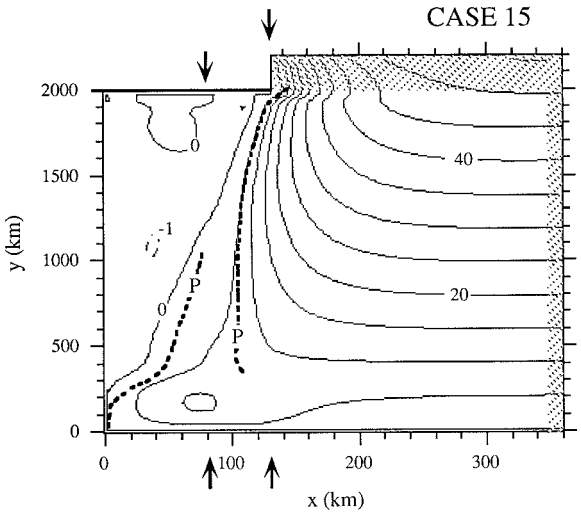

FIG. 10. Flow pattern for case 15. No-slip condition is given at the coast. The shelf width is 80 km.

examined. The balance in cases 11 and 12 is similar to case 2. The balance in case 15 is shown in Fig. 12. Case 14 shows similar balance. Between $y = 1000$ and 1400 km, the flow is accelerated by the pressure gradient, while the acceleration is smaller and given by both pressure gradient and Coriolis force in case 2. In terms of the ageostrophic force in (8), the boundary current is accelerated by the profile term [the second term, F, in (8)]. This fact is seen by the inshore shear zone of the boundary current, which narrows downstream as shown by Fig. 13. It is partly canceled by the crossing term that is reduced by the path's crossing the slope less. Namely, the path control by the crossing term, as in case 2, is modified by a narrowing inshore shear zone.

The vorticity balance on the path is examined. In cases 11 and 12, it is similar to case 2; both the beta and the viscosity produce positive advection. In cases 14 and 15, all terms are small on the offshore paths. In these wide shelf cases the advection is small. Therefore, the path is close to an f/H contour as in linear studies.

The position where the flow is detached from the coastline is examined. The maximum velocities around the detachments are 1.39, 1.37, and 1.37 m s^{-1} in cases 1, 11, and 12, respectively. It is because the path is controlled so that the velocity change is small. This makes the conditions around the detachments similar. So, the positions of the detachments are controlled by the paths, which agree across the shelf/slope among these cases. In the case with a wide shelf, the path that is controlled so that the velocity change is small never meets the coastline. In this case, the flow is detached from the coastline immediately. The maximum velocity

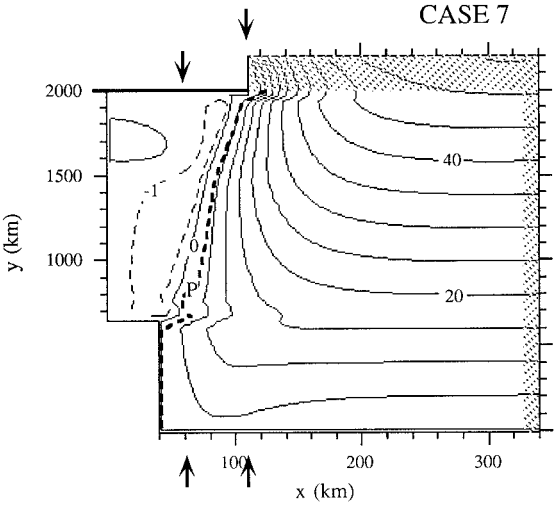

FIG. 9. Flow pattern for case 7. Free-slip condition is given at the coast. The shelf width is 20 km in $y = 0 \sim 640$ km, and 60 km in $y = 640 \sim 2000$ km.

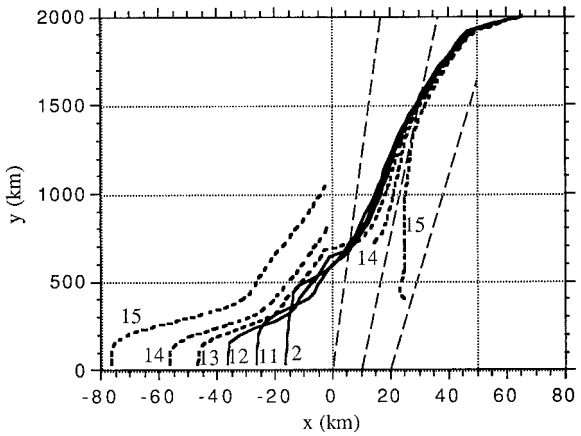

FIG. 11. Paths for the cases with no-slip condition and various shelf width. The vertical broken lines show both ends of the slope. The tilted broken lines are contours of f/H. The path is drawn when the velocity exceeds 0.2 m s^{-1}.

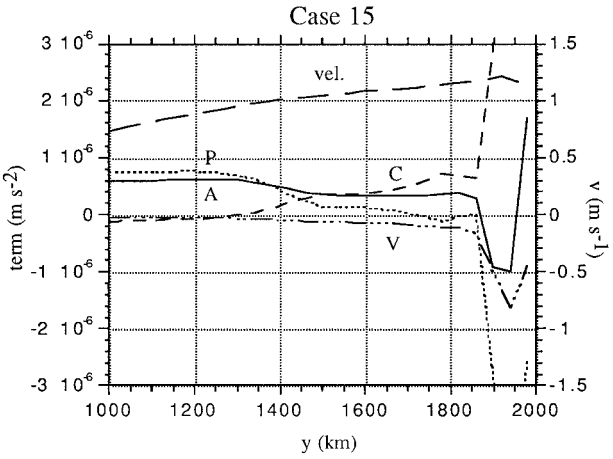

FIG. 12. Alongpath momentum balances on the paths for case 15. The advection (A), the pressure gradient (P), the Coriolis acceleration (C), and the viscosity (V) are shown. The velocity (vel.) on the path is shown, too.

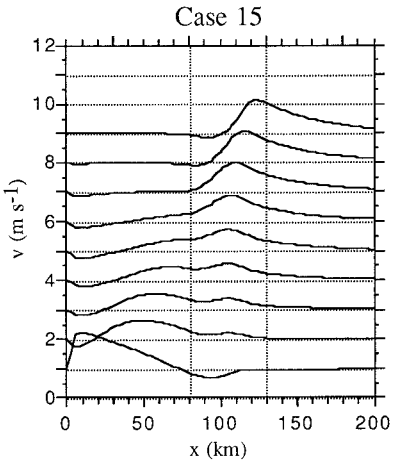

FIG. 13. Profiles of the northward velocity v in east–west sections for cases 15. The sections lie every 200 km from $y = 1800$ (top) to 200 km (bottom).

around the detachment decreases with increasing shelf width; it is 1.33, 1.29, and 1.22 m s^{-1} in cases 13, 14, and 15 respectively. The flow seems to have a minimum distance along the coast that is required for detachment.

Distribution of the potential vorticity of case 15 is shown in Fig. 14. Two regions, A and B in Fig. 14, with uniform potential vorticity are found. Both have closed streamlines. They seem like regions of homogenized potential vorticity (Rhines and Young 1982). Region A corresponds to linear portions of the velocity profiles (Fig. 13) from $y = 800$ to 1600 km. When the shelf is wide so that the path of the cases with narrow shelves does not meet the coastline, part of the inshore region is filled with closed circulations in which the potential vorticity is uniform. The circulations are required to make dynamic balances of both momentum and potential vorticity. They seem to be adjusted so that the path on the slope is close to a contour of f/H because a similar path is found in the cases with the free-slip coast although states of inshore circulations differ, as will be mentioned.

The critical shelf width L_{C1} that divides the classifications is considered. The path of the inviscid model is consistent with the cases with a narrow shelf because the velocity change along the path is small. So, we take ''the maximum width that makes the path of the inviscid model of Nishigaki (1995) meet the coastline'' as the critical width. For parameters of the numerical study, it is 41 km, which is consistent with the calculated paths.

d. Dependence on the shelf width for the free-slip boundary condition

Cases with various shelf widths are presented for the free-slip boundary condition in order to examine how far the boundary current comes inshore and how the path depends on the shelf width. It is found that flow patterns for various shelf widths can be classified into two groups again. In case 23, with a narrow shelf, the flow along the coastline carries all of the gyre volume transport as in case 6. In cases 24 and 25, with wider shelves, the flow patterns are drastically different as in Fig. 15 (case 25). A jet is found on the slope other than a flow along the coastline. The jet on the slope carries most of the gyre transport. Two isolated circulations, A and B (Fig. 15), are found on the shelf/slope. A southward countercurrent lies between them. Paths of the jets on the slope for cases 24 and 25, which have jets on the slope, are shown in Fig. 16 together with the cases 2 and 15 (cases with no-slip condition). The paths are close to a contour of f/H as in case 15. In the alongpath momentum balance of case 25, the pressure gradient accelerates the flow while the Coriolis force and the

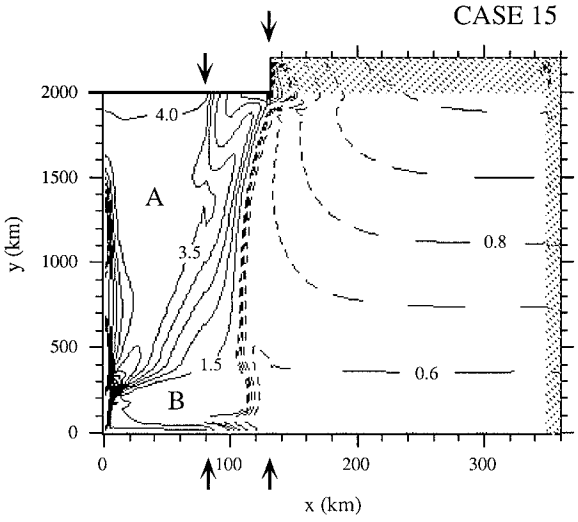

FIG. 14. Distribution of the potential vorticity for case 15. No-slip condition is given at the coast. The shelf width is 80 km.

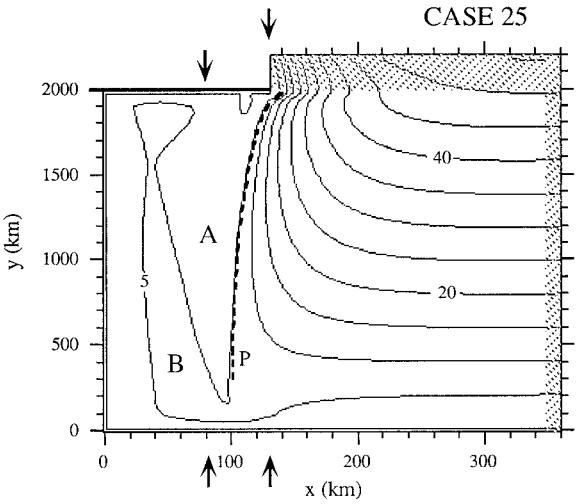

FIG. 15. Flow pattern for case 25. Free-slip condition is applied at the coast. The shelf width is 80 km.

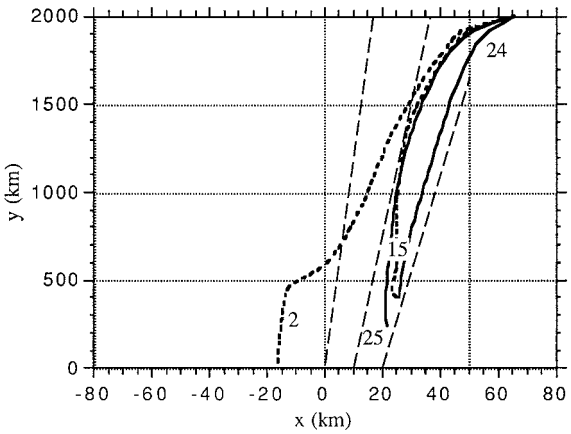

FIG. 16. Paths for the cases with the free-slip condition that have jets on the slope. The paths of the cases with the no-slip condition, cases 2 and 15, are shown by broken lines. The shelf is 60 and 80 km in cases 24 and 25, respectively. The path is drawn when the velocity exceeds 0.2 m s^{-1}.

viscosity are small as in case 15. It comes from the northward pressure gradient force along the coast that breaks (8), whereas the second term of (8) supports the acceleration in case 15.

The vorticity balance on the path is examined. In cases 24 and 25, the viscosity gives positive vorticity while the beta is small. In these cases, the advection is canceled by the viscosity and the beta remains small. Therefore, the path is closer to an f/H contour again. The beta is smaller in case 24, consistent with the fact that the path is closer to an f/H contour in that case.

The potential vorticity distribution of case 25 is shown in Fig. 17. The potential vorticity is not uniform in the isolated circulations A and B: it is maximum in A and minimum in B. The potential vorticity of A comes from the north free-slip boundary, on which relative vorticity is zero and potential vorticity equals f/H, and is modified by the viscosity working on the jet on the slope. The potential vorticity of B comes from the south free-slip boundary. That the path is close to case 15 suggests that the isolated circulations are adjusted so that the path is close to an f/H contour.

The critical shelf width that divides the classifications is considered with the inviscid model. The case with a narrow shelf makes a flow pattern very similar to the inviscid inertial boundary layer that has no stagnant region. The flow patterns of the inviscid cases are shown in Fig. 18 for shelf widths of 20 and 80 km. In the former, all the streamlines come from the inflow at the east end. In the latter, however, streamlines that are not connected to the east inflow are found in the northern part of the slope. This flow pattern is invalid because the governing equation means that the potential vorticity is conserved along streamlines and is applicable only to streamlines that come from the east inflow. This occurs when the width exceeds 58 km, which is consistent with the numerical flow patterns. When the shelf is wide, no flow pattern like Fig. 18b is made because it is impossible to support the potential vorticity in northern closed streamlines. Therefore, isolated circulations are required to make a balance of potential vorticity. The critical width L_{C2} for the free-slip condition means ''the maximum width that makes all the streamlines of the inertial boundary layer connected to the east inflow.''

e. Critical shelf widths

We examine how the critical shelf widths depend on parameters of the subtropical gyre and the bottom topography. Three nondimensional parameters are required: the planetary vorticity gradient β, the inflow u_0 at the east end, and the depth h_S of the shelf. They are defined by

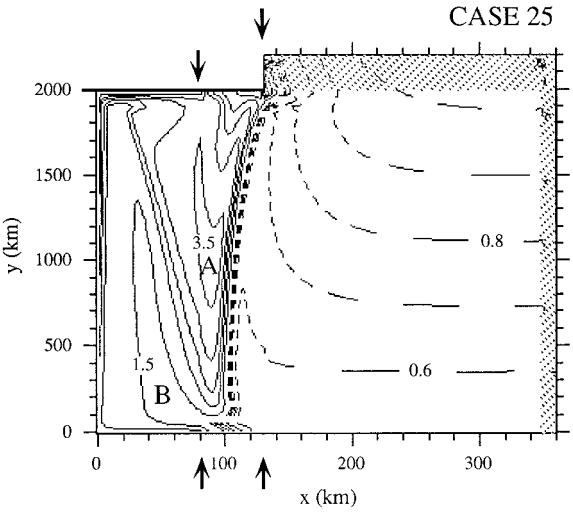

FIG. 17. Distribution of the potential vorticity for case 25. Free-slip condition is applied at the coast. The shelf is 80-km width.

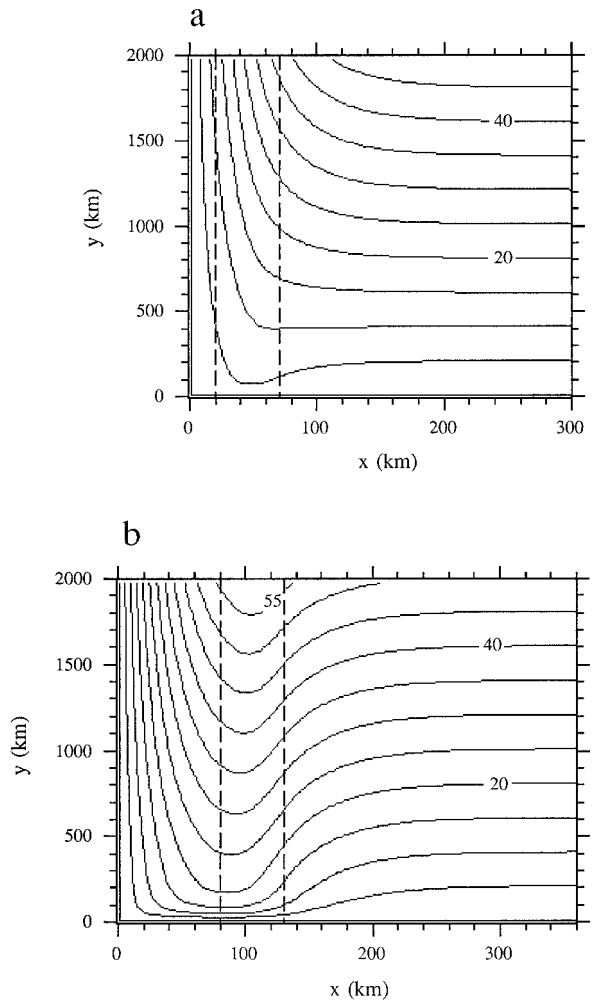

FIG. 18. Flow patterns of the inertial western boundary layers that have no stagnant region. The broken lines show both ends of the slope. The shelf widths are 20 km in (a) and 80 km in (b).

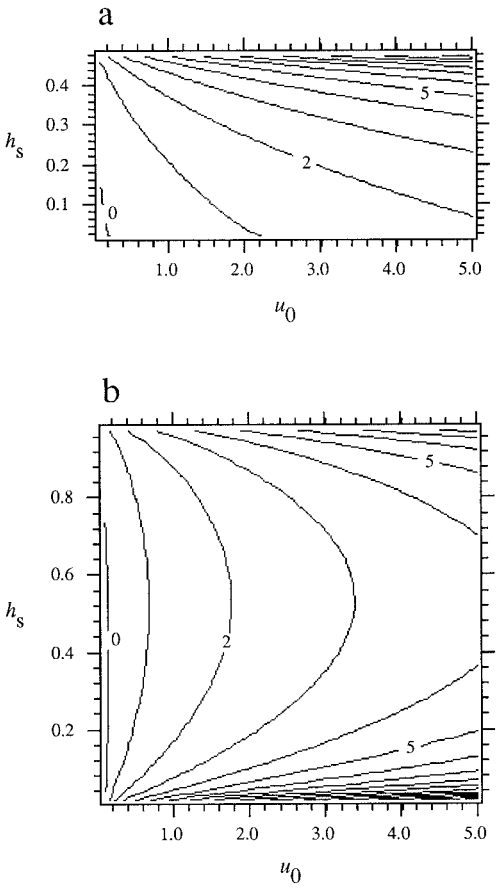

FIG. 19. The critical shelf width L_{C1} (a) and L_{C2} (b) versus the inflow velocity u_0 and the shelf depth h_S. The width is nondimensionalized by the slope width. Here, L_{C1} is for no-slip boundary condition and L_{C2} for free-slip.

$$\beta \equiv \frac{\beta_0 L_Y}{f_0}, \qquad u_0 \equiv \frac{U_0}{\beta_0 L_S^2} = \left(\frac{L_1}{L_s}\right)^2,$$
$$h_S \equiv \frac{H_S}{H_0}, \tag{9}$$

where L_Y is the meridional size of the basin, L_S is the width of the slope, and H_S and H_0 are the depths of the shelf and the open ocean, respectively. Increasing u_0 means not only increasing the volume transport of the gyre but also decreasing the width of the slope L_S with the transport unchanged. The parameters of the numerical model make $\beta = 1.0$, $u_0 = 0.60$, and $h_S = 0.25$.

The critical width L_{C1} for the no-slip condition is calculated for various nondimensional inflow velocities u_O and the shelf depths h_S and shown in Fig. 19a, where the planetary vorticity gradient β is equal to 1.0. It is nondimensionalized by the width of the slope. The calculation is based on the inviscid model of the inertial boundary layer with a velocity front: it is the path of the inviscid case at $y = 0$. How to calculate the path is described in Nishigaki (1995). No critical width exists when $h_S \geq 0.5$: the path of the inviscid case reaches the coastline instead of being trapped by the bottom slope. Here L_{C1} is large when the transport is large because the inertial boundary layer is wide. It is large when the shelf is deep because of the following reason. The velocity must be constant on the path. It is supported by the effect of the bottom slope on continuity; namely, the velocity is afforded by a small volume transport when the depth is shallow. So, the path must be inshore in order to increase the effect of the bottom topography when the shelf is deep.

The other critical width L_{C2} for the free-slip condition for various u_0 and h_S is shown in Fig. 19b, where β is equal to 1.0. It is calculated based on the inertial boundary layer; ''the maximum width that makes all the streamlines connected to the east inflow'' is taken. It is large for large u_0 because the width of the inertial boundary layer is large. It is minimum when the shelf depth is around half of the interior ocean. This dependence is

TABLE 3. Conclusions on how the path of the western boundary current is determined. [a] Conclusions of Nishigaki (1995). [b] The path is controlled by the restoring effect of the ageostrophic component so that the velocity variation on the path is small. [c] Two jets are found on the shelf and the slope. The path on the slope is close to an *f/H* contour. [d] Two jets are found along the coastline and on the slope. The path on the slope is close to an *f/H* contour. [e] Inshore shear zone of the boundary current expands downstream, which is canceled by the path crossing the slope abruptly in terms of the alongpath momentum.

Viscosity	Coastal condition	Width	Boundary current path
None	Stagnant region	$<L_{C1}$	Control by the stagnant region[a]
		$>L_{C1}$	(no solution)[a]
	No stagnant region	$<L_{C2}$	Along the coastline[a]
		$>L_{C2}$	(no solution)
Weak	No-slip	$<L_{C1}$	Control by the ageostrophic force[b]
		$>L_{C1}$	Close to the *f/H* contour[c]
	Free-slip	$<L_{C2}$	Along the coastline
		$>L_{C2}$	Close to the *f/H* contour[d]
Intermediate	No-slip	$<L_{C1}$	Widening shear zone[e]

a result of two effects: (i) when the shelf is deep enough, the countercurrent on the slope is not made because the topographic beta is small and (ii), when the shelf is shallow enough, the countercurrent on the slope is not formed because volume transport on the shelf is small.

4. Summary

We investigate how horizontal viscosity and inshore conditions affect the path of the inertial western boundary current of the subtropical gyre on the bottom slope using steady flow patterns of a numerical model. This study is an extension of the ''inviscid inertial boundary layer model with a velocity front'' (Nishigaki 1995) to cases with viscosity. Conclusions of the inviscid study of Nishigaki and this study on ''how the path of the subtropical inertial western boundary current on the bottom slope is determined'' are summarized in Table 3.

The horizontal viscosity makes a cyclonic shear zone on the inshore flank of the boundary current instead of the velocity front in the inviscid model. In the weakly viscous case, the boundary current follows the coastline at first, then leaves the coast to cross the shelf/slope offshore. The path of the boundary current (the line of maximum velocity) is almost independent of the viscous coefficient and consistent with the inviscid case. Analysis of the alongpath momentum balance reveals that the path is controlled by a restoring effect of the ageostrophic force (sum of the pressure gradient and the Coriolis force) in this case, where the inshore shear zone is thin and a region with weak motion is found inshore of the shear zone. In the intermediately viscous case, the boundary current leaves the coast farther downstream and then crosses the shelf/slope more abruptly. In this case, the inshore shear zone is expanded downstream and no inshore region with weak motion is found. This decreases the ageostrophic force, which is partly canceled by the viscous term and the increase of the ageostrophic force due to the path crossing the slope abruptly.

The stress at the coastal boundary affects the flow pattern of the overall western boundary layer. When a no-slip condition is given, the flow along the coastline in the southern part is separated from the coast by the negative momentum and the positive vorticity supplied by the coastal stress and then turns offshore. When a free-slip condition is given, the flow along the coastline reaches the northern end without leaving the coast. The boundary current for the free-slip condition is drastically different from that for the no-slip condition when the shelf is narrow as in Table 3.

Critical shelf widths are found for both no-slip and free-slip boundary conditions. For each condition, the nature of the boundary current changes across the critical width. Each critical width means the maximum width that enables a type of flow pattern for each condition to fill the whole western boundary layer. The critical shelf width L_{C1} for the no-slip boundary condition is the maximum width for which the flow pattern of the ''inertial boundary layer with a velocity front'' can fill the whole region. When the width is narrower than L_{C1}, the boundary current path across the shelf/slope is determined independent of the shelf width or the coastal position. The boundary current along the coastline in the south part leaves the coast where the path meets the coastline. When the width is wider than L_{C1}, the flow along the coastline leaves the coast immediately and turns offshore. However, another jet is found on the slope, which carries most of the volume transport of the gyre. Here, L_{C1} is large when the gyre transport is large and the shelf is deep. The critical shelf width L_{C2} for the free-slip condition is the maximum width for which the flow pattern of the inertial boundary layer with no stagnant region is possible. When the shelf is narrower than L_{C2}, the boundary current follows the coastline and carries all of the gyre transport. When the shelf is wider than L_{C2}, other than the flow along the coastline, a jet on the slope is found, which carries most of the gyre transport. Here L_{C2} is large when the gyre transport is large and minimum when the shelf depth is around half of the interior ocean.

Isolated circulations appear in the cases of wide

shelves for both boundary conditions. They are required to make balances of momentum and potential vorticity in the whole region. The boundary currents on the slope tend to follow f/H contours and cross the shelf/slope only slightly. It seems that the states of the closed circulations are adjusted so that the paths follow f/H contours.

Acknowledgments. The author thanks Dr. Norihisa Imasato of Kyoto University for his careful and helpful discussions and critical reading of the manuscript. Two reviewers are acknowledged for their helpful suggestions and comments, which improved the manuscript considerably.

APPENDIX

Ageostrophic Component of the Alongpath Momentum

The ageostrophic component is defined by the sum of the pressure gradient and the Coriolis force. We assume that 1) the momentum balance in x is geostrophic and that 2) the pressure gradient along the coast is negligible. The spatial scale and the velocity are much larger in y than in x in our numerical model. This leads to a geostrophic momentum balance in x and an ageostrophic one in y. So, assumption 1) is applicable. Assumption 2) is applicable to cases 1–3, in which a region with weak motion is made inshore of the boundary current. In case 4, the ageostrophic term is modified by a pressure gradient on the coastline as will be mentioned later. The pressure p_p on the path is, with assumption 2,

$$p_P = \int_0^{x_P} fv\, dx, \tag{A1}$$

where subscript P means value on the path. Therefore, the pressure gradient force is, omitting planetary vorticity gradient β_0 and considering assumption 2,

$$-p_{P\eta} = -\int_0^{x_P} fv_\eta\, dx, \tag{A2}$$

where η is the coordinate parallel to the path. The Coriolis term is

$$\begin{aligned} -fu^* &= \frac{f\psi_\eta}{H_P} \\ &= \frac{f}{H_P}\int_0^{x_P} H_\eta v\, dx + \frac{f}{H_P}\int_0^{x_P} Hv_\eta\, dx, \end{aligned} \tag{A3}$$

where u^* is the velocity component normal to the path, in which offshore flow is defined as positive, and ψ is the streamfunction. Therefore, the ageostrophic component is

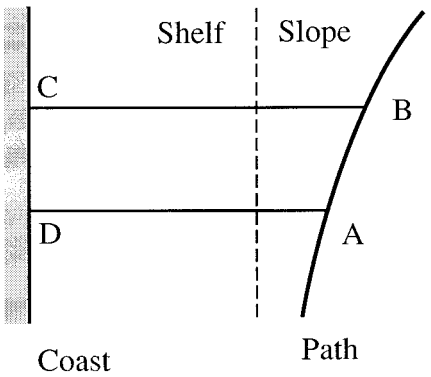

FIG. A1. A circuit to consider the momentum balance.

$$\begin{aligned} -p_{P\eta} - fu^* &= \frac{f}{H_P}\int_0^{x_P} H_\eta v\, dx \\ &\quad - \frac{f}{H_P}\int_0^{x_P} (H_P - H)v_\eta\, dx \\ &\equiv X + F. \end{aligned} \tag{A4}$$

This comes from a discrepancy between the velocity and the volume transport, which is made by the bottom topography. The first term X of (A4) is the crossing term made by the inshore shear zone crossing the slope. Suppose the velocity profile is the same between two cross sections, DA and CB in Fig. A1. This makes no pressure difference between A and B. The volume transport is larger across DA because of the bottom topography. This leads to an inshore flow across the path AB and downstream Coriolis force. So, positive ageostrophic force is produced. The second term F of (A4) is the profile term, which originates from the alongpath change of the velocity profile in the inshore shear zone. Suppose the velocity is increasing downstream: the volume transport due to the velocity increase is compensated by an inshore flow across the path AB. The compensating velocity is smaller than one expected from the velocity difference between DA and CB because the depth is greater on AB. This makes the Coriolis term smaller than the pressure gradient. So, negative ageostrophic force is made.

The crossing term X has a restoring effect to the change of path orientation. When the crossing is made more abrupt, the velocity tends to decrease downstream because the depth increase along the path becomes larger. However, X tends to accelerate the flow more. This works as a restoring effect to the path change and controls the path so that the velocity variation along the path is small. Although F also has a restoring effect through the magnitude of the velocity, it is smaller in amplitude.

REFERENCES

Cessi, P., 1991: Laminar separation of colliding western boundary currents. *J. Mar. Res.*, **49,** 697–717.

——, R. V. Condie, and W. R. Young, 1990: Dissipative dynamics of western boundary currents. *J. Mar. Res.*, **48,** 677–700.
Chapman, D. C., and K. H. Brink, 1987: Shelf and slope circulation induced by fluctuating offshore forcing. *J. Geophys. Res.*, **92** (C11), 11 741–11 759.
Charney, J. G., 1955: The Gulf Stream as an inertial boundary layer. *Proc. Natl. Acad. Sci. USA,* **41,** 731–740.
Dengg, J., 1993: The problem of Gulf Stream separation: A barotropic approach. *J. Phys. Oceanogr.,* **23,** 2182–2200.
Fofonoff, N. P., 1954: Steady flow in a frictionless homogeneous ocean. *J. Mar. Res.*, **13,** 254–262.
Haidvogel, D. B., J. C. McWilliams, and P. R. Gent, 1992: Boundary current separation in a quasigeostrophic, eddy resolving ocean circulation model. *J. Phys. Oceanogr.,* **22,** 882–902.
Holland, W. R., 1967: On the wind-driven circulation in an ocean with bottom topography. *Tellus,* **19,** 582–600.
Leaman, K. D., E. Jones, and T. Rossby, 1989: The average distribution of volume transport and potential vorticity with temperature at three sections across the Gulf Stream. *J. Phys. Oceanogr.,* **19,** 36–51.
Morgan, G. W., 1956: On the wind-driven ocean circulation. *Tellus,* **3,** 301–320.
Munk, W. H., 1950: On the wind-driven ocean circulation. *J. Meteor.*, **7,** 79–93.
Nishigaki, H., 1995: Inertial boundary layer with a velocity front: How the bottom slope controls the western boundary current path. *J. Phys. Oceanogr.,* **25,** 216–225.
Rhines, P. B., and W. R. Young, 1982: Homogenization of potential vorticity in planetary gyres. *J. Fluid Mech.,* **122,** 347–367.
Richardson, W. S., W. S. Schmitz, and P. Niiler, 1969: The velocity structure of the Florida Current from Florida Straits to Cape Fear. *Deep-Sea Res.*, **16** (Suppl.), 225–231.
Salmon, R., 1992: A two-layer Gulf Stream over a continental slope. *J. Mar. Res.*, **50,** 341–365.
Schmitz, W. J., Jr., and P. P. Niiler, 1969: A note on the kinetic energy exchange between fluctuations and mean flow in the surface layer of the Florida Current. *Tellus,* **21,** 814–819.
Stommel, H., 1948: The westward intensification of wind-driven ocean currents. *Trans. Amer. Geophys. Union,* **99,** 202–206.